Optical Control of Initialization of a Quantum Dot in the Voigt Geometry near a Graphene Layer

DIONISIS STEFANATOS, VASILIOS KARANIKOLAS, NIKOS ILIOPOULOS, EMMANUEL PASPALAKIS
University of Patras
Department of Materials Science
265 04 Rio Patras
GREECE
dionisis@post.harvard.edu, karanikv@tcd.ie, n.iliopoulos@windowslive.com, paspalak@upatras.gr

Abstract: We propose and analyze fast spin initialization for a quantum dot in the Voigt geometry by placing it near a graphene layer. We show that high levels of fidelity, significantly larger than in the case of the quantum dot without the layer, can be quickly obtained due to the anisotropy of the enhanced spontaneous decay rates of the quantum dot near the graphene layer. We initially obtain these results by using a continuous wave optical field with constant control amplitude. We also use state of the art numerical optimal control to find the time-dependent electric field which maximizes the final fidelity for the same short duration as in the previous case. A better fidelity is obtained with this method.

Key–Words: Quantum control, numerical optimal control, quantum dot, spin initialization, Voigt geometry, optical pumping, spin dynamics

1 Introduction

Semiconductor quantum dots (QDs) are among the most promising candidates for solid state quantum information processing and for quantum technologies in general since they allow for engineered energies and wavefunctions and can be efficiently manipulated by electric, magnetic and optical fields [1, 2]. They can also be integrated with microphotonic and nanophotonic structures, such as microcavities and nanocavities, photonic crystals, and plasmonic nanostructures, allowing for extra control in both the weak and strong light-matter coupling regimes. Spin states in negatively and positively charged QDs are especially useful for quantum information technologies, with the important problems being the spin initialization, coherent manipulation, and readout. A QD structure that has been studied in detail both theoretically and experimentally is based on the spin states in the Voigt configuration, where a magnetic field is applied perpendicular to the growth axis of the QD [1, 2, 3, 4, 5, 6, 7, 8, 9, 10].

The level structure for the QD in the Voigt geometry is shown in Fig. 1(a). The natural initial state of the QD is an incoherent mixture with equal populations in the two electron spin states, states $|1\rangle$ and $|2\rangle$. A basic process in quantum information protocols is the initialization [11], where in this system a specific electron spin state is created. The most common method for initialization relies on the optical pumping process [3]. Let's assume that we wish to create state $|2\rangle$. We apply an optical field with a $x-$polarized electric field which couples spin state $|1\rangle$ to the trion state $|4\rangle$. Then, by spontaneous decay the population is pumped into spin state $|2\rangle$ after a few decay times. In an isotropic photonic environment, for example in free-space vacuum, the decay rates from state $|4\rangle$ to states $|1\rangle$ and $|2\rangle$ are the same. By using an anisotropic photonic environment the decay rate from state $|4\rangle$ to state $|2\rangle$ increases in comparison to the decay rate from state $|4\rangle$ to state $|1\rangle$ and this leads to preferential deexcitation towards state $|2\rangle$ in shorter times. This idea has been explored by embedding the QD in a micropillar [5], placing it in photonic crystal nanocavities [6], next to a metallic nanoparticle [7], a metal-dielectric interface [8], and even a bowtie nanoantenna [9].

Here, we explore a different nanostructure for accelerating the optical pumping process in a QD in the Voigt geometry. We place the QD next to a single graphene layer, see Fig. 1(b). Graphene strongly modifies the spontaneous decay rates of nearby quantum emitters [12, 13, 14, 15]. It can also create anisotropic spontaneous decay rates for nearby quantum emitters for dipoles parallel and perpendicular to the graphene sheet [12, 14, 15]. In the present work we investigate the dynamics of spin initialization for the composite system using optical pumping with two different types of optical pulses, using typ-

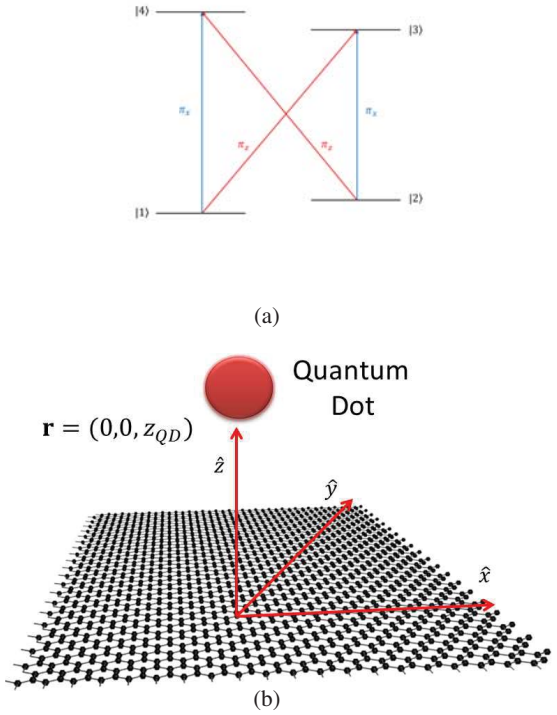

Figure 1: (a) Energy level diagram for a QD in the Voigt geometry. The magnetic field induces the Zeeman splitting in the upper and lower levels. The optical field resonant with the $|1\rangle \leftrightarrow |4\rangle$ transition is x-polarized. (b) The QD is placed a distance $z = R$ above a graphene layer, which lies on the $x - y$ plane at $z = 0$. The growth axis of the QD is y while the magnetic field is applied along the x-axis.

ical values of energies for the QD. First, we use a continuous wave electromagnetic field with constant Rabi frequency, and show that, in the presence of the graphene layer, higher fidelity levels can be achieved in short times compared to the case without graphene. Next, we use state of the art numerical optimal control to find the time-dependent electric field, leading to a time-dependent Rabi frequency profile, which maximizes the final fidelity for the same short duration as in the previous case. A better fidelity is obtained with this method.

2 Dynamics equations for a quantum dot in the Voigt geometry near a graphene monolayer

For the studied system, we consider a singly-charged self-assembled QD grown along the y-axis. By applying an external magnetic field in the Voigt geometry, along the x-axis, lifts the degeneracy of electron/hole levels by Zeeman splitting. Then, the ground spin levels are $|1\rangle = |\downarrow_x\rangle$ and $|2\rangle = |\uparrow_x\rangle$ and the two excited trion states are $|3\rangle = |\downarrow_x\uparrow_x\Uparrow_x\rangle$ and $|4\rangle = |\downarrow_x\uparrow_x\Downarrow_x\rangle$. Here, $\Uparrow$ ($\Downarrow$) and $\uparrow$ ($\downarrow$) denote heavy hole and electron spins, respectively. For the level scheme, see Fig. 1(a). Here, the vertical transitions ($|1\rangle \leftrightarrow |4\rangle$ and $|2\rangle \leftrightarrow |3\rangle$) give x-polarized dipole matrix elements and the cross transitions ($|1\rangle \leftrightarrow |3\rangle$ and $|2\rangle \leftrightarrow |4\rangle$) give z-polarized dipole matrix elements. In this work, we aim to create state $|2\rangle$. Thus, we take the QD to interact with a x-polarized laser field applied at exact resonance with the $|1\rangle \leftrightarrow |4\rangle$ transition, exploring the method of optical pumping.

In order to study the dynamics of spin initialization, we derive the density matrix equations of the system. The Hamiltonian describing the interaction between the optical field and the QD system, in the dipole and rotating wave approximations, is

$$\begin{aligned} H &= \sum_{n=1}^{4} \hbar\omega_n |n\rangle\langle n| \\ &- \hbar\left[\Omega(t)e^{-i\omega_0 t}|4\rangle\langle 1| + \Omega(t)e^{-i\omega_0 t}|3\rangle\langle 2|\right] \\ &+ \text{H.c.} \end{aligned} \quad (1)$$

where $\hbar\omega_n, n = 1, 2, 3, 4$, is the energy of state $|n\rangle$ and $\Omega(t)$ is the generally time-dependent Rabi frequency of the applied field. The field is resonant with the $|1\rangle \leftrightarrow |4\rangle$ transition, thus $\omega_0 = \omega_4 - \omega_1 = \omega_{41}$. Here we use the value $\hbar\omega_0 = 1.31$ eV. This is a typical value for InAs self-assembled QDs used in relevant studies [3, 4, 9], and it is also adopted here. We note that although we did not calculate the electronic structure of the QD numerically here, one can calculate its electronic structure using several methods, like the effective mass approximation and $\mathbf{k} \cdot \mathbf{p}$ method [16], empirical tight binding models [17], empirical pseudopotential based approaches [18], and others [19]. Using the unitary operator $U(t) = e^{-i\sum_{n=1}^{4} a_n |n\rangle\langle n| t}$, with $a_1 = \omega_1$, $a_2 = \omega_0 + \omega_1$, $a_3 = \omega_3 + \omega_0 - \omega_{41}$, $a_4 = \omega_0 + \omega_1$, Hamiltonian (1) is transformed to the interaction Hamiltonian

$$\begin{aligned} H_{eff} &= -\hbar(\omega_0 - \omega_{21})|2\rangle\langle 2| - \hbar(\omega_0 - \omega_{41})|3\rangle\langle 3| \\ &-\hbar(\omega_0 - \omega_{41})|4\rangle\langle 4| - \hbar\Big[\Omega(t)|4\rangle\langle 1| \\ &+\Omega(t)e^{-i(\omega_0+\omega_{43})t}|3\rangle\langle 2| + \text{H.c.}\Big], \end{aligned} \quad (2)$$

where $\omega_{nm} = \omega_n - \omega_m$. Note that $\hbar\omega_{21}, \hbar\omega_{43}$ are the Zeeman splittings of the single-electron spin states and the heavy-hole spin trion states, respectively. Throughout this article we use the values $\hbar\omega_{21} = 0.124$ meV, $\hbar\omega_{43} = 0.078$ meV [4].

Using the above Hamiltonian we can easily obtain the equations of motion for the density matrix elements of the QD. In the case where the laser frequency is at exact resonance with the transition $|1\rangle \leftrightarrow |4\rangle$, these are

$$\dot{\rho}_{11} = \gamma_{41}\rho_{44} + \gamma_{31}\rho_{33} - 2\Omega\rho_{41}^I, \quad (3)$$

$$\dot{\rho}_{22} = \gamma_{32}\rho_{33} + \gamma_{42}\rho_{44} + 2\Omega\tilde{\rho}_{23}^I, \quad (4)$$

$$\dot{\rho}_{33} = -(\gamma_{31}+\gamma_{32})\rho_{33} - 2\Omega\tilde{\rho}_{23}^I, \quad (5)$$

$$\dot{\rho}_{44} = -(\gamma_{41}+\gamma_{42})\rho_{44} + 2\Omega\rho_{41}^I, \quad (6)$$

$$\dot{\rho}_{41}^I = -\frac{\gamma_{41}+\gamma_{42}}{2}\rho_{41}^I + \Omega(\rho_{11}-\rho_{44}), \quad (7)$$

$$\dot{\tilde{\rho}}_{23}^R = -\frac{\gamma_{31}+\gamma_{32}}{2}\tilde{\rho}_{23}^R + (\omega_{21}+\omega_{43})\tilde{\rho}_{23}^I, \quad (8)$$

$$\dot{\tilde{\rho}}_{23}^I = -\frac{\gamma_{31}+\gamma_{32}}{2}\tilde{\rho}_{23}^I - (\omega_{21}+\omega_{43})\tilde{\rho}_{23}^R + \Omega(\rho_{33}-\rho_{22}), \quad (9)$$

where $\tilde{\rho}_{23} = \rho_{23}e^{-i(\omega_{41}+\omega_{43})t}$ and the superscripts R, I denote real and imaginary parts, respectively. Note that in the above equations we have also incorporated the spontaneous emission from the upper to the lower energy levels, with

$$\gamma_{41} = \gamma_{32} = \gamma_x = F_x\gamma, \quad \gamma_{42} = \gamma_{31} = \gamma_z = F_z\gamma \quad (10)$$

being the radiative decay rates of the corresponding QD transitions modified by the coupling between the QD and the graphene layer.

3 Fast initialization with optical control

As we have already mentioned above, the natural initial state of the system is an equal incoherent mixture of states $|1\rangle$ and $|2\rangle$, thus $\rho_{11}(0) = \rho_{22}(0) = 1/2$ while the populations of the rest levels and the coherence terms are all zero. Starting from this initial state, the goal is to apply the appropriate optical field in order to quickly prepare the spin state $|2\rangle$ with high fidelity. In the following we separately investigate how this can be efficiently achieved with constant control Ω and with time-dependent control $\Omega(t)$.

3.1 Constant Rabi frequency

We consider a specific case where the QD is placed a distance $R = 5$ nm above the graphene layer, while the chemical potential of the layer is set to the value $\mu = 1$ eV. We also consider that the layer is placed in a dielectric environment with $\varepsilon_1 = \varepsilon_2 = 4$. Note that dielectric environments with permittivity value 4 have been considered in other works that study the spontaneous decay of quantum emitters near graphene layers

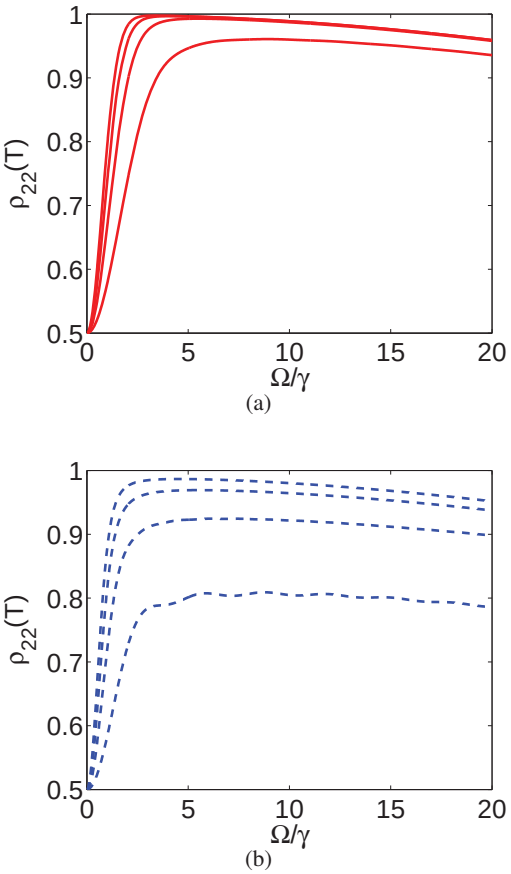

Figure 2: Final population of level $|2\rangle$, $\rho_{22}(T)$, versus the constant control Ω for four durations $T = 1/\gamma, 2/\gamma, 3/\gamma, 4/\gamma$ (from bottom to top) and: (a) in the presence of a graphene layer placed a distance $R = 5$ nm from the QD with chemical potential $\mu = 1$ eV, (b) in the absence of the graphene layer. A realistic dielectric environment with $\varepsilon_1 = \varepsilon_2 = 4$ is considered in both cases.

[13], as they model very well the permittivity values of several materials that are used as hosts to graphene, like hBN, GaN and SiO_2. With the above parameter values one can calculate the corresponding Purcell factors using electromagnetic theory, and specifically the method of scattering superposition, see Ref. [14] for the details of the method. The resulting values are $F_x = 3.99307$ and $F_z = 6.00242$. Using these values we solve numerically Eqs. (3)-(9) and simulate the response of the quantum dot system. In Fig. 2(a) we plot the final population of level $|2\rangle$, $\rho_{22}(T)$, versus the constant control Ω for four durations $T = 1/\gamma, 2/\gamma, 3/\gamma, 4/\gamma$ (from bottom to top). For comparison, in Fig. 2(b) we plot the final populations obtained in the absence of graphene, where $F_x = F_z = 2$, for the same durations (again with in-

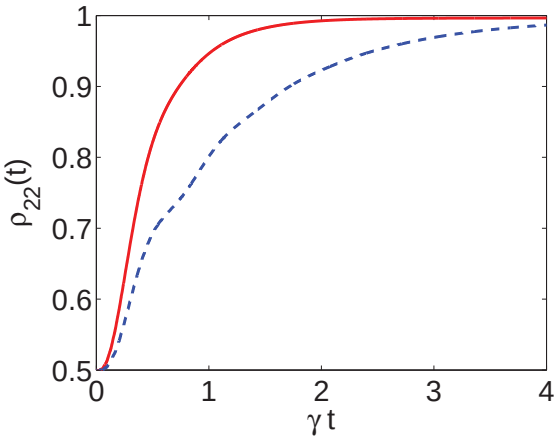

Figure 3: Time evolution of state $|2\rangle$ population $\rho_{22}(t)$ when a constant Rabi frequency $\Omega = 5\gamma$ is applied, for a realistic dielectric environment with $\varepsilon_1 = \varepsilon_2 = 4$ and (a) in the presence of a graphene layer of chemical potential $\mu = 1$ eV placed a distance $R = 5$ nm from the QD (red solid line), (b) in the absence of a graphene layer (blue dashed line). Observe that the fidelity obtained with the layer is larger than the one without it.

creasing duration from bottom to top). Obviously, the anisotropy in the Purcell factors induced by the presence of the graphene layer results in higher initialization fidelities which are obtained at earlier times. This is further illustrated in Fig. 3, where we display the time evolution of the population $\rho_{22}(t)$ in the presence (red solid line) and in the absence (blue dashed line) of graphene, for a constant control $\Omega = 5\gamma$ (a value close to optimal as shown in Fig. 2) and duration $T = 4/\gamma$. For example, at $t = 3/\gamma$ the value $\rho_{22}(3/\gamma) = 0.9962$ is obtained with graphene, while the corresponding value without graphene is just 0.9691. This kind of improvement is quite important for quantum information processing applications, where large values of fidelity close to unity are necessary.

3.2 Time-dependent Rabi frequency

Here we recourse to numerical optimization to obtain time-dependent controls $\Omega(t)$ which are zero at the initial and final times

$$\Omega(0) = \Omega(T) = 0, \tag{11}$$

while maximize the final population of level $|2\rangle$. This kind of controls are more appropriate for experimental implementation, since they avoid the initial and final jumps of the square pulse.

In order to find $\Omega(t)$, we use the freely available optimal control solver BOCOP [20], which can

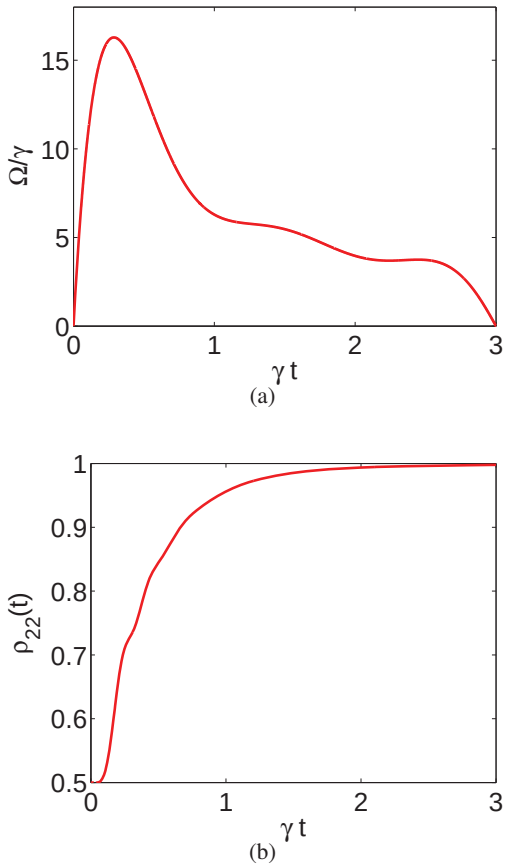

Figure 4: For a realistic dielectric environment with $\varepsilon_1 = \varepsilon_2 = 4$, a graphene layer with chemical potential $\mu = 1$ eV placed a distance $R = 5$ nm from the QD, and duration $T = 3/\gamma$: (a) Optimal control $\Omega(t)$ using a polynomial of order $p = 6$ in Eq. (12), (b) corresponding $\rho_{22}(t)$. The final value $\rho_{22}(T) = 0.9979$ is larger than the value 0.9962 obtained with constant control and for the same duration in Fig. 3.

easily incorporate boundary conditions like (11). We also exploit a feature provided by this program, which allows to express the control as a polynomial function of time. Specifically, we consider Ω as an extra state variable, on which we impose boundary conditions (11), while we place the polynomial control in its derivative. The corresponding equation in normalized time $\tau = \gamma t$ is

$$\frac{d}{d\tau}\left(\frac{\Omega}{\gamma}\right) = \sum_{k=0}^{p} a_k \tau^k, \tag{12}$$

where we have used a p-th order polynomial for the derivative, so Ω is of order $p+1$, and a_k are the dimensionless unknown coefficients to be determined by the optimization procedure. We additionally impose the

Table 1: Optimal coefficients $a_k, k = 0, 1, \ldots p$, for the polynomial control (14) with $p = 6$, when $\mu = 1$ eV, $R = 5$ nm, $\varepsilon_1 = \varepsilon_2 = 4$, and the duration is set to $T = 3/\gamma$.

$a_k, p = 6$
146.2137
-907.9316
1812.3362
-1688.2531
806.7791
-191.4565
17.8462

constraint

$$0 \leq \Omega(t)/\gamma \leq 20, \tag{13}$$

in order to restrict the field amplitude within experimentally feasible values. Now we can state the optimal control problem. For system equations (3)-(9), which can easily be expressed using normalized time and dimensionless variables, augmented by Eq. (12) for Ω, we would like to find the coefficients a_k which maximize the final value $\rho_{22}(T)$ for a specific duration T, while satisfy the boundary condition (11) and the constraint (13). Having found a_k we can integrate Eq. (12) and obtain the field

$$\frac{\Omega(t)}{\gamma} = \sum_{m=1}^{p+1} \frac{a_{m-1}}{m} (\gamma t)^m \tag{14}$$

expressed in the original time t.

As in the case with constant control, we consider a specific example with $\mu = 1$ eV, $R = 5$ nm, $\varepsilon_1 = \varepsilon_2 = 4$, while the duration is set to $T = 3/\gamma$. The optimal coefficients found using BOCOP for polynomial of order $p = 6$ in Eq. (12) are listed in Table 1. The resulting control field $\Omega(t)$ and the corresponding evolution $\rho_{22}(t)$ are displayed in Fig. 4. The final value $\rho_{22}(T)$ is 0.9979, larger than the value 0.9962 obtained with constant control $\Omega = 5\gamma$ for the same duration in Fig. 3, as expected from an optimization procedure. Note that if we increase the polynomial order in the control, for example to $p = 7$, a marginal improvement in the fidelity at the fifth decimal digit is observed, and this is why we use the value $p = 6$ in Eq. (12).

The suggested methodology is advantageous compared to other recent works where control fields polynomial in time with coefficients optimized with respect to an objective are used, see for example Refs. [21, 22, 23]. In these studies, some of the coefficient are fixed in order to satisfy the boundary conditions at initial and final times. For each value of the remaining free coefficients, the system equations are simulated and the resulting objective value is recorded. The optimal coefficients are those optimizing the objective. Usually, one or two free coefficients are employed, since the number of simulations and thus the computational time grows exponentially with the number of free parameters. With the optimal control solver BOCOP that we exploit here, we can use a large number of coefficients in the optimization, as we did for $p = 6$, while the optimal solution is obtained much faster than with the above described practice. Finally, note that instead of polynomial control functions we could have used trigonometric functions, as did for a different problem in a recent publication [24].

4 Conclusion

We studied the problem of fast spin initialization for a QD in the Voigt geometry placed near a graphene layer. We showed that high levels of fidelity, significantly larger than in the case of the QD without the layer, can be quickly obtained due to the anisotropy of the enhanced spontaneous decay rates of the QD near the graphene layer. We obtained this improvent by first using a continuous wave electromagnetic field with constant control amplitude. Next, we used state of the art numerical optimal control to find the time-dependent electric field which maximized the final fidelity for the same short duration as in the previous case. A better fidelity was obtained with this method. Closing, we would like to point out that a full parametric study of the initialization dynamics for various distances between the QD and the graphene layer, the constant Rabi frequency and the chemical potential of the graphene is needed and we have started working on it.

Acknowledgements: The research is implemented through the Operational Program "Human Resources Development, Education and Lifelong Learning" and is co-financed by the European Union (European Social Fund) and Greek national funds (project EΔBM34, code MIS 5005825).

References:

[1] R. J. Warburton, Single spins in self-assembled quantum dots, *Nat. Mater.* 12, 2013, pp. 483–493.

[2] W. B. Gao, A. Imamoglu, H. Bernien, and R. Hanson, Coherent manipulation, measurement and entanglement of individual solid-state spins using optical fields, *Nat. Photon.* 9, 2015, pp. 363–373.

[3] C. Emary, X. Xu, D. G. Steel, S. Saikin, and L. J. Sham, Fast initialization of the spin state of an electron in a quantum dot in the Voigt configuration, *Phys. Rev. Lett.* 98, 2007, art. no. 047401.

[4] S. E. Economou and T. L. Reinecke, Theory of fast optical spin rotation in a quantum dot based on geometric phases and trapped states, *Phys. Rev. Lett.* 99, 2007, art. no. 217401.

[5] V. Loo, L. Lanco, O. Krebs, P. Senellart, and P. Voisin, Single-shot initialization of electron spin in a quantum dot using a short optical pulse, *Phys. Rev. B* 83, 2011, art. no. 033301.

[6] A. Majumdar, P. Kaer, M. Bajcsy, E. D. Kim, K. G. Lagoudakis, A. Rundquist, and J. Vuckovic, Proposed coupling of an electron spin in a semiconductor quantum dot to a nanosize optical cavity, *Phys. Rev. Lett.* 111, 2013, art. no. 027402.

[7] M. A. Antón, F. Carreño, S. Melle, O. G. Calderón, E. Cabrera-Granado, and M. R. Singh, Optical pumping of a single hole spin in a p-doped quantum dot coupled to a metallic nanoparticle, *Phys. Rev. B* 87, 2013, art. no. 195303.

[8] Y. Peng, Z.-Y. Yun, Y. Liu, T.–S. Wu, W. Zhang, and H. Ye, Fast initialization of hole spin in a quantum dot-metal surface hybrid system, *Physica B* 470–471, 2015, pp. 1–5.

[9] F. Carreño, F. Arrieta-Yáñez, and M. A. Antón, Spin initialization of a p-doped quantum dot coupled to a bowtie nanoantenna, *Opt. Commun.* 343, 2015, pp. 97–106.

[10] E. Paspalakis, S. E. Economou, and F. Carreño, Adiabatically preparing quantum dot spin states in the Voigt geometry, *J. Appl. Phys.* 125, 2019, art. no. 024305.

[11] D. P. DiVincenzo, The physical implementation of quantum computation *Fortsch. Phys.* 48, 2000, pp. 771–783.

[12] F. H. L. Koppens, D. E. Chang, and F. J. García de Abajo, Graphene plasmonics: a platform for strong lightmatter interactions, *Nano Lett.* 11, 2011, pp. 3370–3377.

[13] G. W. Hanson, E. Forati, W. Linz, and A. B. Yakovlev, Excitation of terahertz surface plasmons on graphene surfaces by an elementary dipole and quantum emitter: Strong electrodynamic effect of dielectric support, *Phys. Rev. B* 86, 2012, art. no. 235440.

[14] V. Karanikolas and E. Paspalakis, Plasmon-induced quantum interference near carbon nanostructures, *J. Phys. Chem. C* 122, 2018, pp. 14788-14795.

[15] W. Fang, G.–X. Li, and Y. P. Yang, Controllable radiation properties of a driven exciton-biexciton quantum dot couples to a graphene sheet, *Opt. Express* 26, 2018, pp. 29561–29587.

[16] P. Harrison, *Quantum Wells, Wires and Dots: Theoretical and Computational Physics of Semiconductor Nanostructures*, 3^{rd} Edition, Wiley, 2009.

[17] C. Delerue and M. Lannoo, *Nanostructures: Theory and Modelling*, Springer, 2004.

[18] G. Bester, Electronic excitations in nanostructures: an empirical pseudopotential based approach *J. Phys.: Condens. Matter* 21, 2009, art. no. 023202.

[19] S. M. Reimann and M. Manninen, Electronic structure of quantum dots *Rev. Mod. Phys.* 74, 2002, pp. 1283–1342.

[20] F. Bonnans, P. Martinon, D. Giorgi, V. Grélard, S. Maindrault, and O. Tissot, *BOCOP: an open source toolbox for optimal control*, (INRIA-Saclay, Ile de France, 2017).

[21] M. Palmero, S. Wang, D. Guéry-Odelin, J.–S. Li, and J. G. Muga, Shortcuts to adiabaticity for an ion in a rotating radially-tight trap, *New J. Phys.* 18, 2016, art. no. 043014.

[22] Q. Zhang, X. Chen, and D. Guéry-Odelin, Reverse engineering protocols for controlling spin dynamics, *Sci. Rep.* 7, 2017, art. no. 15814.

[23] Y. Yan, Y.–C. Li, A. Kinos, A. Walther, C. Shi, L. Rippe, J. Moser, S. Kröll, and X. Chen, Inverse engineering of shortcut pulses for high fidelity initialization on qubits closely spaced in frequency, *Opt. Express* 27, 2019, pp. 8267–8282.

[24] D. Stefanatos and E. Paspalakis, Efficient generation of the triplet Bell state between coupled spins using transitionless quantum driving and optimal control, *Phys. Rev. A* 99, 2019, art. no. 022327.